

# Improvement of Near-field Tsunami Forecasting Method Using Ocean Bottom Pressure Sensor Network (S-net)

Yuichiro Tanioka (✉ [tanioka@sci.hokudai.ac.jp](mailto:tanioka@sci.hokudai.ac.jp))

---

## Full paper

**Keywords:** tsunami forecasting method, data assimilation, tsunami numerical simulation, Kurile subduction zone

**Posted Date:** June 26th, 2020

**DOI:** <https://doi.org/10.21203/rs.3.rs-37911/v1>

**License:** © ⓘ This work is licensed under a Creative Commons Attribution 4.0 International License.

[Read Full License](#)

---

**Version of Record:** A version of this preprint was published on September 14th, 2020. See the published version at <https://doi.org/10.1186/s40623-020-01268-1>.

1 **Improvement of Near-field Tsunami Forecasting Method Using Ocean Bottom Pressure**  
2 **Sensor Network (S-net)**

3 Yuichiro Tanioka<sup>1</sup>

4 <sup>1</sup> Institute of Seismology and Volcanology, Hokkaido University, N10W8 Kita-ku Sapporo,  
5 Hokkaido 060-0810, Japan.

6  
7 **Abstract**

8 Since the installation of a dense cabled observation network around the Japan Trench (S-net) by  
9 the Japanese government that includes 150 sensors, several tsunami forecasting methods that use  
10 the data collected from the ocean floor sensors were developed. One of such methods is the  
11 tsunami forecasting method which assimilates the data without any information of earthquakes.  
12 The tsunami forecasting method based on the assimilation of the ocean-bottom pressure data  
13 near the source area was developed by Tanioka in 2018. However, the method is too simple to be  
14 used for an actual station distribution of S-net. To overcome its limitation, we developed an  
15 interpolation method to generate the appropriate data at the equally spaced positions for the  
16 assimilation from the data observed at sensors in S-net. The method was numerically tested for  
17 two large underthrust fault models, a giant earthquake (Mw8.8) and the Nemuro-oki earthquake  
18 (Mw8.0) models. Those fault models off Hokkaido in Japan are expected to be ruptured in the  
19 future. The weighted interpolation method, in which weights of data are inversely proportional to  
20 the square of the distance, showed good results for the tsunami forecast method with the data  
21 assimilation. Furthermore, results indicated that the method is applicable to the actual observed  
22 data at the S-net stations. The only limitation of the weighted interpolation method is that the  
23 computed tsunami wavelengths tend to be longer than the actual tsunamis wavelength.

24

25 **Keywords:**

26 tsunami forecasting method, data assimilation, tsunami numerical simulation, Kurile subduction  
27 zone.

28

29 **1. Introduction**

30 The 2011 Tohoku-oki earthquake (Mw9.0) generated a large tsunami along the Pacific coast  
31 of northern Japan (Mori et al., 2012). Although the Japan Meteorological Agency (JMA) issued a  
32 major tsunami warning along the Pacific coast of Japan immediately after the earthquake (Ozaki,  
33 2011), the tsunami caused a catastrophic disaster with approximately 19,000 casualties. After  
34 this event, the development of a more accurate and rapid tsunami warning system became a high-  
35 priority focus area in Japan.

36 For this purpose, the Japanese government installed a dense cabled observation network,  
37 called the seafloor observation network for earthquakes and tsunami around the Japan Trench (S-  
38 net), in 2017. The network is operated by the National Research Institute for Earth Science and  
39 Disaster Resilience (NEID). In this network, 150 observation stations consisting of ocean-bottom  
40 pressure sensors and seismometers are connected by cables at the 30-km intervals (Uehira et  
41 al.,2012; Kanazawa, 2013). The cables are distributed on the seafloor offshore off northern Japan  
42 (Figure 1).

43 Recently, various early forecasting methods for tsunami using the dense seafloor observation  
44 networks have been proposed. Tsushima et al. (2012) developed a method called Tsunami  
45 Forecasting based on Inversion for initial sea Surface Height (tFISH) which estimates the initial  
46 sea surface deformation from tsunami waveforms observed at ocean bottom pressure gauges.

47 Yamamoto et al. (2016) developed a tsunami forecasting method that rapidly estimates tsunami  
48 inundation based on a multi-index method and compares the observed tsunami heights with the  
49 pre-computed tsunami heights at ocean bottom sensors. Moreover, new tsunami computation  
50 methods based on the assimilation of tsunami observations without the tsunami source  
51 information were developed by Maeda et al., (2015), Tanioka (2018), and Tanioka and Gusman  
52 (2018). In particular, the near-field tsunami inundation forecasting method developed by Tanioka  
53 and Gusman (2018) uses the time derivative of the pressure waveforms observed at the ocean  
54 bottom pressure sensors near the source area. Therefore, accurate tsunami computation can be  
55 performed without any tsunami source information as soon as the earthquake or tsunami  
56 generation is completed. Tanioka and Gusman (2018) also tested ocean-bottom pressure sensors  
57 equally distributed at 15 min intervals or approximately 30 km apart. In reality, the S-net ocean-  
58 bottom sensors are not installed at uniform intervals (Figure 1), particularly in the north-south  
59 direction, and have a lesser number than those tested by Tanioka and Gusman (2018). They  
60 finally concluded that it is necessary to improve their method by using the exact locations of the  
61 S-net sensors for real time tsunami inundation forecasts.

62 In this paper, we improve the tsunami forecasting method proposed by Tanioka (2018) and  
63 Tanioka and Gusman (2018) to be able to use the exact locations of the S-net sensors. This  
64 improved method was tested for two expected large underthrust earthquakes off the Pacific coast  
65 of Hokkaido, Japan: an expected magnitude 9 class earthquake, and the Nemuro-oki earthquake  
66 with a magnitude of 8.

67

## 68 **2. Previous Method to Determine the Tsunami Height Field**

69 Tanioka (2018) presented a tsunami simulation method that assimilates dense ocean bottom  
70 pressure data near the tsunami source regions. Tanioka and Gusman (2018) suggested a near-  
71 field tsunami inundation forecasting method based on the method presented by Tanioka (2018).  
72 Here, we briefly explain the method used to determine the tsunami height field. A governing  
73 equation for the tsunami propagation, the wave equation of the linear shallow-water  
74 approximation, is as follows:

$$75 \quad \frac{\partial^2 h_f(x,y,t)}{\partial t^2} = \frac{\partial^2 \eta(x,y,t)}{\partial t^2} = gd \left( \frac{\partial^2 \eta(x,y,t)}{\partial x^2} + \frac{\partial^2 \eta(x,y,t)}{\partial y^2} \right), \quad (1)$$

76 where  $d$  is the depth of the ocean,  $\eta(x, y, t)$  is the ocean surface displacement or tsunami height  
77  $h_f(x, y, t)$  is the water depth fluctuation proportional to the ocean-bottom pressure change  
78  $\Delta p(x, y, t)$  as:  $h_f(x, y, t) = \frac{1}{\rho g} \Delta p(x, y, t)$  where  $\rho$  is the density of sea water and  $g$  is the  
79 gravitational acceleration. From Eq. (1) the finite difference equation is obtained as follows:

$$80 \quad \frac{h_{f,i,j}^{k+1} - 2h_{f,i,j}^k + h_{f,i,j}^{k-1}}{\Delta t^2} = gd_{i,j} \left( \frac{\eta_{i+1,j}^k - 2\eta_{i,j}^k + \eta_{i-1,j}^k}{\Delta x^2} + \frac{\eta_{i,j+1}^k - 2\eta_{i,j}^k + \eta_{i,j-1}^k}{\Delta y^2} \right), \quad (2)$$

81 where  $i$  and  $j$  are indices of points for the x- and y-directions in the computed domain,  $k$  is the  
82 index for time steps,  $\Delta x$  and  $\Delta y$  are the spacing intervals in the x and y directions, respectively,  
83 and  $\Delta t$  is the time interval. Afterwards, we assumed that there were ocean bottom pressure  
84 sensors at each point (marked in red dots in Figure 2). The spacing interval for both the x and y  
85 directions is 10 arc-min or approximately 18 km. As such, the total number of sensors was  
86 assumed to be 275. The left-hand side of Eq. (2) was obtained from the observed pressure data at  
87 each ocean bottom pressure sensor. The unknown parameters were ocean surface displacement  
88 field or tsunami height field,  $\eta_{i,j}^k$ , above each ocean-bottom pressure gauge at a particular time,  $k$ .  
89 The tsunami heights outside the pressure gauge network were assumed to be 0. Subsequently, we

90 were able to compute the tsunami height field,  $\eta_{i,j}^k$ , above the ocean bottom pressure sensor  
 91 network by solving Eq. (2) for all ocean bottom pressure sensors by using the inversion  
 92 technique as described by Tanioka (2018).

93

### 94 3. Interpolation Method for Data Assimilation

95 A problem with the method mentioned above is that in practice, the S-net sensors are not  
 96 distributed at the 10 arc-min intervals in the x and y direction, and the number of the S-net  
 97 sensors is much less than 275 (Figure 2). To solve this problem, we need to develop an  
 98 appropriate interpolation method to obtain pressure data at the points situated at the 10 arc-min  
 99 intervals (red dots in Figure 2) from the observed pressure data at the S-net sensors (black dots in  
 100 Figure 2). A number of weighted interpolation methods were tested to find the most appropriate

101 one. The left-hand side of Eq. (2),  $z_p^k = \frac{h_f^{k+1} - 2h_f^k + h_f^{k-1}}{\Delta t^2}$ , at each sensor position  $(x_p, y_p)$  in S-net

102 was calculated from the observed pressure data. The left-hand side of Eq. (2),  $z_{i,j}^k =$

103  $\frac{h_{f_{i,j}}^{k+1} - 2h_{f_{i,j}}^k + h_{f_{i,j}}^{k-1}}{\Delta t^2}$ , at each point  $(x_{i,j}, y_{i,j})$  at the 10 arc-min intervals (red dots in Figure 2) was

104 obtained by the weighted interpolation equation as

105 follows:

$$z_{i,j}^k = \frac{\sum_{p=1}^n w_{p,i,j} z_p^k}{\sum_{p=1}^n w_{p,i,j}} \quad (3)$$

106

107

108 where  $w_{p,i,j}$  is the weight factor for each observed point  $(p)$  to calculate  $z_{i,j}^k$  at each point  $(i, j)$ .

109 Then, the weight factor was defined as follows:

$$w_{p,i,j} = \frac{1}{\left( \sqrt{(x_p - x_{i,j})^2 + (y_p - y_{i,j})^2} \right)^\alpha} \quad (4)$$

110

111 where  $\alpha$  is the control factor. If control factor  $\alpha$  equals one, the weights are inversely  
112 proportional to the distance between the observed points in S-net and points for assimilation. In  
113 this study, we varied control factor  $\alpha$  from 1 to 3 (integers only) to find the best factor that  
114 provides an appropriate tsunami height distribution near a tsunami source area using the  
115 assimilation technique developed by Tanioka (2018).

116

#### 117 **4. Test Region and Fault Models**

118 Great underthrust earthquakes repeatedly occurred in the past at the plate interface in the  
119 subduction zone where the Pacific plate subducts beneath the Kurile trench off Hokkaido (Figure  
120 1). Historically, the Pacific coast of Hokkaido has suffered from large disasters due to those  
121 earthquakes and their associated tsunamis (Tanioka et al., 2007). Additionally, the paleo-  
122 earthquake studies using tsunami deposits along the Pacific coast of Hokkaido revealed that  
123 much larger tsunamis repeatedly occurred in the past 6000 years compared with historical  
124 tsunamis (Nanayama et al., 2003; Hirakawa et al., 2005). The most recent large paleo-tsunami  
125 that occurred in the early 17<sup>th</sup> century (Figure 1) was well studied by Satake et al., (2008) and  
126 Ioki and Tanioka (2016). The fault model of the earthquake was constructed by reproducing the  
127 observed tsunami deposit distribution along the Hokkaido coast with the computed one. Ioki and  
128 Tanioka (2016) concluded that the great underthrust earthquake with a moment magnitude of 8.8  
129 ruptured a large area of the plate interface off Hokkaido. The Headquarters for Earthquake  
130 Research Promotion, Japan, published a long-term evaluation report on the occurrence of large  
131 subduction earthquakes along the Kurile trench (Headquarters of Earthquake Research  
132 Promotion, 2018). They reported that the probability of a giant earthquake with a magnitude  
133 exceeding Mw 8.8 along the Kurile trench in 30 years is between 7% and 40%. Therefore,

134 mitigation of tsunami disasters due to the giant earthquake (M8.8) has become an urgent  
135 challenge in Japan, particularly in Hokkaido.

136 In this study, we chose the hypothetical giant earthquake (Mw8.8) along the Kurile trench off  
137 Hokkaido to test our tsunami simulation by assimilating pressure data observed by the S-net  
138 sensors near the source region. The fault length and fault width for this hypothetical earthquake  
139 (Figure 2) were set to be 300 km and 100 km, respectively, as per the estimations of the 17<sup>th</sup>-  
140 century giant earthquake fault model (Satake et al., 2008; Ioki and Tanioka, 2016). A strike of  
141 228°, a dip of 15°, and a rake of 90° were set to be the same as those in the 17<sup>th</sup>-century giant  
142 earthquake fault model (Table 1). A slip amount was calculated to be 15 m by assuming a  
143 moment magnitude of 8.8 and a rigidity of  $4 \times 10^{10}$  N/m<sup>2</sup>.

144 The Headquarters for Earthquake Research Promotion also reported that the probability of a  
145 great Nemuro-oki earthquake (Mw7.8-8.5) along the Kurile trench in 30 years is approximately  
146 70%, being higher than that of the giant earthquake (Mw8.8). In this region, the 1973 Nemuro-  
147 oki earthquake (Mw 7.8) (Figure 1) and the 1894 Numuro-oki earthquake (Mw8.2) were  
148 previously occurred. Tanioka et al. (2007) showed that the fault size of the 1894 event (200km x  
149 100 km) was larger than that of the 1973 event (80 km x 80 km). In this study, we chose the  
150 Nemuro-oki earthquake (Mw 8.0) to test our method. The fault length and fault width of the  
151 earthquake (Figure 2) were set to be 100 km and 80 km, respectively. A strike of 240°, a dip of  
152 15°, and a rake of 90° were set the same as those in the fault model of the Nemuro-oki  
153 earthquakes (Table 1). A slip amount was calculated to be 4 m by assuming a moment magnitude  
154 of 8.0 and a rigidity of  $4 \times 10^{10}$  N/m<sup>2</sup>.

155

## 156 **5. Method for Numerical Computation Tests**

157 Two reference tsunamis, used as the original tsunamis for synthetic tests, were computed in  
 158 the area off Hokkaido and Tohoku (Figure 2). The coseismic vertical deformation was calculated  
 159 using the Okada's (1985) equations from the fault models of the two reference earthquakes  
 160 (Table 1) and used as the initial conditions of tsunamis. The tsunamis were numerically  
 161 computed by solving the linear long-wave equations by using the finite difference method with a  
 162 staggered grid system (Satake, 2015). The grid size of the tsunami computation was set at 1 arc-  
 163 min (approximately 1.8 km). The time step of the computation was set to be 2 s to satisfy the  
 164 stability condition. The duration of the earthquake was chosen to be 90 seconds.

165 To test the assimilation method, the tsunami waveforms at the S-net observation points (black  
 166 dots in Figure 2) were computed numerically from the reference fault models and transferred to  
 167 the water-depth fluctuation,  $h_f(x,y,t)$  in Eq. (1), as described in Tanioka (2018). afterwards, the

168 left-hand side of Eq. (2),  $z_p^k = \frac{h_f^{k+1} - 2h_f^k + h_f^{k-1}}{\Delta t^2}$ , at each sensor position  $(x_p, y_p)$  in S-net at a time

169  $k$  was calculated from the water-depth fluctuation data. Time intervals,  $\Delta t$ , for the giant  
 170 earthquake (Mw8.8) and the Nemuro earthquake (Mw8.0) cases were set at 6 s and 30 s,  
 171 respectively, so that term,  $h_f^{k+1} - 2h_f^k + h_f^{k-1}$ , was significant enough to be observed at the S-net

172 sensors. Then, those at equally distributed points  $(x_{i,j}, y_{i,j})$  at the 10 arc-min intervals (red dots in

173 Figure 2),  $z_{i,j}^k = \frac{h_{f_{i,j}}^{k+1} - 2h_{f_{i,j}}^k + h_{f_{i,j}}^{k-1}}{\Delta t^2}$ , were obtained by the above interpolation methods.

174 Subsequently, the tsunami height fields at equally distributed points at a time  $k$  were computed  
 175 using the assimilation method as described by Tanioka (2018). For tsunami simulation, the  
 176 tsunami height field obtained at a time  $k$  from the observed depth fluctuation data at the S-net  
 177 sensors replaced the tsunami height field at a time  $k$  during the tsunami numerical simulation.

178 The replacements of the tsunami height field as data assimilations were completed at 90 s after

179 the initiation of the earthquake as the duration of the earthquake was set at 90 s. Finally, the  
180 tsunami numerical simulation was continued until 90 min after the earthquake by solving the  
181 linear long-wave equations without data assimilation.

182

## 183 **6. Results**

184 In the first test case, a tsunami caused by the giant earthquake (Mw8.8) along the Kurile Trench  
185 off Hokkaido was numerically computed as a reference tsunami. The computed tsunami height  
186 fields at 90 and 1200 s after the initiation of the earthquake are shown in Figure 3. The tsunami  
187 height fields were computed by the assimilation of simulated observation data at sensors in S-net  
188 (Figure 2) using the interpolation method utilized in Eqs. (3) and (4) with three control factors ( $\alpha$   
189 = 1, 2, and 3) (Figure 3). Seven computed tsunami waveforms at Hanasaki, Kushiro, Hiroo, and  
190 Urakawa in Hokkaido, and Hachinohe, Miyako, and Kesenuma in Tohoku obtained from the  
191 reference tsunami and from the assimilations using the interpolation with three control factors ( $\alpha$   
192 =1, 2, and 3) are compared in Figure 4. The maximum tsunami heights at these seven locations  
193 are also presented in Table 2. The tsunami waveforms (Figure 4) and maximum tsunami heights  
194 (Table 2) from the reference tsunami computation were comparable to those from the  
195 assimilation of simulated observation data using the interpolation, where control factor  $\alpha$  equaled  
196 two. The maximum tsunami heights computed from the assimilation of the data using the  
197 interpolation, where control factor  $\alpha$  equaled one, were underestimated compared to the  
198 maximum tsunami heights computed directly from the reference fault model. Some of the  
199 tsunami waveforms from the assimilation of those data were different from those of the reference  
200 model, especially the waveforms at Hanasaki in Hokkaido. On the contrary, the maximum  
201 tsunami heights computed from the assimilation of the data using interpolation, where control

202 factor  $\alpha$  equaled 3, were overestimated in comparison with those computed directly from the  
203 reference fault model. Therefore, we conclude that the weighted interpolation method, where  
204 control factor  $\alpha$  equaled two in Eq. (4), is appropriate for our assimilation method using the  
205 ocean-bottom pressure data observed at the S-net sensors.

206 As for the second test case, the tsunami caused by the fault model of the Nemuro-oki  
207 earthquake (Mw 8.0) was numerically computed as a reference tsunami. The computed tsunami  
208 height fields at 90 and 1200 s after the initiation of the earthquake are shown in Figure 5a. The  
209 tsunami height fields were computed by the assimilation of simulated observation data at the S-  
210 net sensors (Figure 2) using the interpolation method as described by Eq. (3), where control  
211 factor  $\alpha$  equaled two (Figure 5b). Seven computed tsunami waveforms from the reference  
212 tsunami and from the data assimilations using the interpolation are compared in Figures 6a-b.  
213 The maximum tsunami heights at these seven locations are also presented in Table 3. As the  
214 assimilation area was much larger than the source area in this case, small tsunami height fields in  
215 the southwest of the assimilation area, where no tsunami was computed as a reference tsunami,  
216 were realized for the data assimilation (Figure 5b). Therefore, the computed tsunami waveforms  
217 from the data assimilation using the interpolation (Figure 6b) have longer period characteristics  
218 and higher maximum tsunami heights than those waveforms of the reference tsunami. These  
219 results indicate that the data assimilation area needs to be limited to an area with reasonable  
220 water depth fluctuations observed at the S-net sensors.

221 Furthermore, we used a small assimilation area shown in Figure 7. For sensors in this small  
222 assimilation area, the calculated assimilation data  $z_p^k = \frac{h_f^{k+1} - 2h_f^k + h_f^{k-1}}{\Delta t^2}$  were more than 1/20 of  
223 the maximum assimilation data of all the sensors. The computed tsunami height fields at 90 and  
224 1200 s after the initiation of the earthquake are shown in Figure 5c. Figure 6 shows that seven

225 computed tsunami waveforms from the reference tsunami are better fitted by the computed  
226 tsunami waveforms from the data assimilation in the small area using interpolation than in the  
227 large area. Table 3 also shows that the maximum tsunami heights of the reference tsunami better  
228 agree with those computed from the data assimilation in the small area than in the large area.

229

## 230 **7. Discussion and Conclusion**

231 Overall, we showed that the tsunami height fields of the reference tsunami could be modeled  
232 from the assimilation of data obtained from observed data at the S-net sensors by the  
233 interpolation method as described in Eq. (3), where control factor  $\alpha$  equaled two. However, the  
234 wavelengths of tsunami waveforms computed using the assimilation of data obtained from the  
235 data at the sensors by the interpolation method were longer than those of the reference tsunami,  
236 especially for the Nemuro-oki earthquake (Mw8.0). This indicates the limitation of data  
237 assimilation using the suggested interpolation method because assimilation data at 176 points  
238 (red dots in Figure 7) were calculated from the interpolation of data at only 12 S-net sensors for  
239 the Nemuro-oki earthquake case. Therefore, tsunami height fields from a smaller earthquake are  
240 more difficult to be computed using our data assimilation method.

241 Herein, we developed a tsunami forecasting method using the assimilation of data obtained by  
242 interpolation of observed data at the S-net sensors near the tsunami source area. The  
243 interpolation method, as described in Eq. (3), where control factor  $\alpha$  equaled two, performed  
244 acceptable for the tsunami forecasting method presented in this study. For an earthquake with a  
245 magnitude of 8, such as the Nemuro-oki earthquake (Mw8.0), the assimilation area should be  
246 limited to an area where the reliable water depth fluctuations are observed at the S-net sensors. In  
247 addition, we concluded that tsunami wavelengths computed using our present interpolation

248 method tend to be longer than those of actual tsunamis which serves as a limitation of this  
249 method.

250

### 251 **Acknowledgments**

252 We would like to thank Editage ([www.editage.com](http://www.editage.com)) for English language editing. This study was  
253 supported by JSPS KAKENHI Grant Number 18H03819.

254

### 255 **Availability of data and materials:**

256 None

### 257 **Competing interests:**

258 None

### 259 **Funding**

260 This study was supported by JSPS KAKENHI Grant Number 18H03819.

261 This study was also supported by the Ministry of Education, Culture, Sports, Science and  
262 Technology (MEXT) of Japan, under its The Second Earthquake and Volcano Hazards  
263 Observation and Research Program (Earthquake and Volcano Hazard Reduction Research)

### 264 **Authors' contributions**

265 Y.T did all.

266

### 267 **References**

268 Headquarters of Earthquake Research Promotion (2018), Evaluations of occurrence potential of  
269 large earthquakes along the Kurile trench, [https://www.jishin.go.jp/main/chousa/kaikou\\_pdf/  
270 chishima3.pdf](https://www.jishin.go.jp/main/chousa/kaikou_pdf/chishima3.pdf) (in Japanese)

271 Hirakawa, K., Y. Nakamura, Y. Nishimura (2005), Mega-Tsunamis since last 6500 years along  
272 the Pacific Coast of Hokkaido, Special Issue, *Chikyu Monthly*, 49, 173-180 (in Japanese)

273 Imamura, F. (1996). Review of tsunami simulation with a finite difference method, in Long-  
274 Wave Runup Models, edited by H. Yeh, P. Liu, and C. Synolakis, 403 pp., *World Scientific*,  
275 Singapore.

276 Ioki, K., and Y. Tanioka (2016), Re-estimated fault model of the 17th century great earthquake  
277 off Hokkaido using tsunami deposit data, *Earth Planet. Sci. Lett.*, 433, 133-138,  
278 <https://doi.org/10.1016/j.epsl.2015.10.009>

279 Kanazawa, T. (2013), Japan Trench earthquake and tsunami monitoring network of cable-linked  
280 150 ocean bottom observatories and its impact to earth disaster science, *Proceedings of the  
281 International Conference Underwater Technology*.

282 Maeda, T., K. Obara, M. Shinohara, T. Kanazawa, and K. Uehira (2015), Successive estimation  
283 of a tsunami wavefield without earthquake source data: A data assimilation approach toward  
284 real-time tsunami forecasting, *Geophys Res Lett*, 42(19), 7923–7932.

285 Mori N, Takahashi T, The 2011 Tohoku earthquake tsunami joint survey group (2012)  
286 Nationwide post event survey and analysis of the 2011 Tohoku earthquake tsunami. *Coastal  
287 Eng J* 54(1):1250001. <https://doi.org/10.1142/S0578563412500015>

288 Nanayama, F., K. Satake, R. Furukawa, K. Shimokawa, B.F. Atwater, K. Shigeno, and S.  
289 Yamaki (2003) Unusually large earthquakes inferred from tsunami deposits along the Kurile  
290 trench, *Nature*, 424, 660-663

291 Okada, Y. (1986). Surface deformation due to shear and tensile faults in a half-space. *Bulletin of*  
292 *the Seismological Society of America*, 75, 1135-1154.

293 Ozaki, T. (2011), Outline of the 2011 off the Pacific coast of Tohoku earthquake (Mw 9.0) -  
294 Tsunami warnings/advisories and observations, *Earth Planets Space*, 63(7), 827– 830

295 Satake, K. (2015). *Tsunamis, in treatise on geophysics, vol 4* (2nd ed., pp. 477–504. Amsterdam:  
296 Elsevier.

297 Satake, K., F. Nanayama, and S. Yamaki (2008), Fault models of unusual tsunami in the 17th  
298 century along the Kurile trench, *Earth Planets Space*, 60, 925-935.

299 Tanioka, Y., K. Satake, and K. Hirata (2007), Recurrence of Recent Large Earthquakes Along  
300 the Southernmost Kurile-Kamchatka Subduction Zone, *Geophysical monograph*, 172, 145-  
301 152.

302 Tanioka, Y. (2018), Tsunami Simulation Method Assimilating Ocean Bottom Pressure Data  
303 Near a Tsunami Source Region, *Pure Appl Geophys*, 175(2), 721–729.

304 Tanioka, Y. and A.R. Gusman, (2018) Near-field tsunami inundation forecast method  
305 assimilating ocean bottom pressure data: A synthetic test for the 2011 Tohoku-oki tsunami,  
306 *Phys. Earth Planet. Int.*, 283, 82-91, <https://doi.org/10.1016/j.pepi.2018.08.006>.

307 Tsushima, H., R. Hino, Y. Tanioka, F. Imamura, and H. Fujimoto (2012), Tsunami waveform  
308 inversion incorporating permanent seafloor deformation and its application to tsunami  
309 forecasting, *J Geophys Res Solid Earth*, 117, B03311, 10.1029/2011JB008877.

310 Uehira, K., Kanazawa, T., Noguchi, S., Aoi, S., Kunugi, T., Matsumoto, T., Okada, Y.,  
311 Sekiguchi, S., Shiomi, K., Shinohara, M., & Yamada, T. (2012). Ocean bottom seismic and

312 tsunami network along the Japan Trench. In: Abstract OS41C-1736 presented at 2012 Fall  
313 Meeting, AGU.

314 Yamamoto, N., S. Aoi, K. Hirata, W. Suzuki, T. Kunugi, and H. Nakamura (2016), Multi-index  
315 method using offshore ocean-bottom pressure data for real-time tsunami forecast, *Earth,*  
316 *Planets and Space*, 68(1), 128, doi:10.1186/s40623-016-0500-7.

317

318

319

320 **Figure Captions:**

321 Figure 1. Bathymetry of the study area and locations of the S-net sensors (red dots). The red  
322 rectangle shows the source area of the 17<sup>th</sup> century giant earthquake (Mw 8,8), according to  
323 Ioki and Tanioka (2016). The black rectangle shows the source area of the 1973 Nemuro-oki  
324 earthquake (Mw7.8), as per Tanioka et al. (2007).

325

326 Figure 2. Tsunami simulation area and locations of the calculated assimilation data (red dots)  
327 using interpolation of the observed data at the S-net sensors (black dots). The blue and green  
328 rectangles show the locations of the two test fault models of the hypothetical giant  
329 earthquake (Mw8.8) and the Nemuro-oki earthquake (Mw8.0), respectively. Triangles  
330 demarcate the locations where the tsunami waveforms are compared in Figures 4 and 6.

331

332 Figure 3. Comparisons of the tsunami height fields 90 and 1200 s after the initiation of the  
333 earthquake for the reference tsunami of the giant earthquake and three assimilation tsunamis

334 as computed by the interpolation of the simulated observation data at the S-net sensors using  
335 Eq. (3), where control factors  $\alpha$  from Eq. (4) ranges from 1 to 3.

336

337 Figure 4. Comparisons of tsunami waveforms at seven locations (refer to Figure 2 for exact  
338 locations) for the reference tsunami of the giant earthquake and three assimilation tsunamis,  
339 where control factors  $\alpha$  from Eq. (4) ranges from 1 to 3.

340

341 Figure 5. Comparisons of tsunami height fields 90 and 1200 s after the initiation of the  
342 earthquake for the reference tsunami (a) of the Nemuro-oki earthquake and two assimilation  
343 tsunamis computed using the interpolation of the simulated observation data at the S-net  
344 sensors for a large assimilation area (b) (for exact locations refer to Figure 2) and a the small  
345 assimilation area (c) (for exact locations refer to Figure 7).

346

347 Figure 6. Comparisons of tsunami waveforms at seven locations (refer to Figure 2 for exact  
348 locations) for the reference tsunami (a) of the Nemuro-oki earthquake case and two  
349 assimilation tsunamis using a large assimilation area (b) (for exact locations refer to Figure 2)  
350 and a the small assimilation area (c) (for exact locations refer to Figure 7).

351

352 Figure 7. Locations of the assimilation data in a small assimilation area (marked by red dots)  
353 calculated by the interpolation of the observed data at the S-net sensors (black dots). The blue  
354 rectangle shows the test fault model of the Nemuro-oki earthquake (Mw8.0). Triangles  
355 demarcate the locations of the tsunami waveforms from Figure 6.

356

357  
358  
359  
360  
361  
362

Table 1. Fault models for the two test earthquakes

Test fault model	Fault length (km)	Fault width (km)	Strike (°)	Dip (°)	Rake (°)	Slip (m)
Giant Eq. (Mw8.8)	300	100	228	15	90	15.0
Neumuro-oki (Mw8.8)	100	80	240	15	90	4.0

363  
364  
365  
366  
367

Table 2. Comparison of the maximum tsunami heights at seven locations computed from the reference tsunami of the giant earthquake (Mw8.8) and the assimilations using the interpolation where control factors  $\alpha$  ranges from 1 to 3 (see Figure 4). The ratios of the maximum tsunami heights are indicated in parentheses.

Location	Reference	$\alpha=1$	$\alpha=2$	$\alpha=3$
	Max. heights (m)	Max. heights, (ratio) (m)	Max. heights, (ratio) (m)	Max. heights, (ratio) (m)
Hanasaki	13.6	3.93, (0.29)	14.2, (1.04)	14.9, (1.10)
Kushiro	10.5	7.99, (0.76)	10.8, (1.03)	15.2, (1.45)
Hiroo	17.8	8.88, (0.50)	21.2, (1.19)	28.0, (1.57)
Urakawa	4.21	1.69, (0.40)	3.96, (0.94)	4.92, (1.17)
Hachinohe	4.40	4.20, (0.95)	7.58, (1.72)	10.3, (2.34)
Miyako	5.79	3.54, (0.61)	6.30, (1.09)	7.99, (1.38)
Kesennuma	2.84	2.80, (0.99)	2.77, (0.98)	3.37, (1.19)
Average	8.45	4.72, (0.64)	9.54, (1.14)	12.1, (1.46)

368  
369  
370  
371  
372

Table 3. Comparison of the maximum tsunami heights at seven locations computed from the reference tsunami of the Nemuro-oki earthquake (Mw8.0) and the assimilations using the large and small assimilation areas (for their location refer to Figure 6). The ratios of the maximum tsunami heights are indicated in parentheses.

Location	Reference	Large assimilation area	Small assimilation area
	Max. heights (m)	Max. heights, (ratio) (m)	Max. heights, (ratio) (m)
Hanasaki	3.58	2.82, (0.79)	2.77, (0.77)
Kushiro	0.94	2.12, (2.26)	1.32, (1.40)
Hiroo	1.33	1.87, (1.41)	1.57, (1.18)
Urakawa	0.35	0.30, (0.86)	0.58, (1.66)
Hachinohe	0.60	1.17, (1.95)	1.12, (1.87)
Miyako	0.88	1.44, (1.64)	1.39, (1.58)
Kesennuma	0.39	1.02, (2.62)	0.78, (2.00)

---

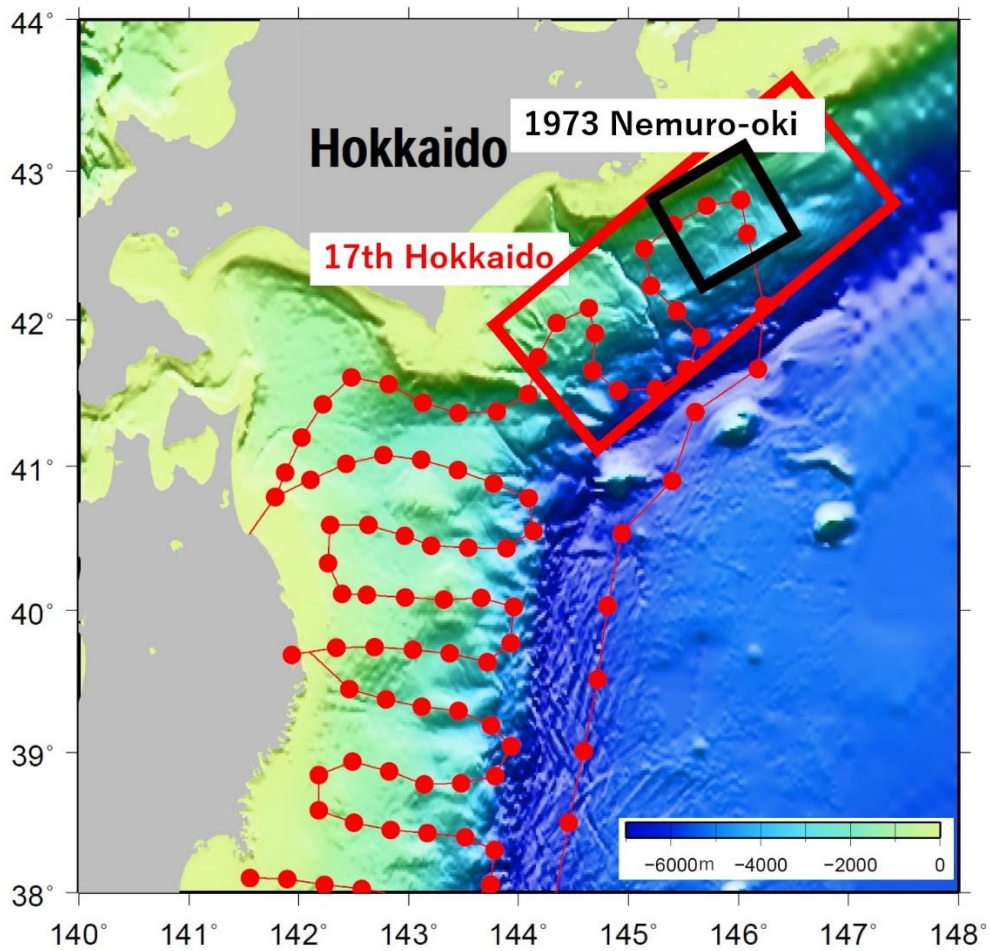
Average	0.98	1.53, (1.65)	1.36, (1.49)
---------	------	--------------	--------------

---

373

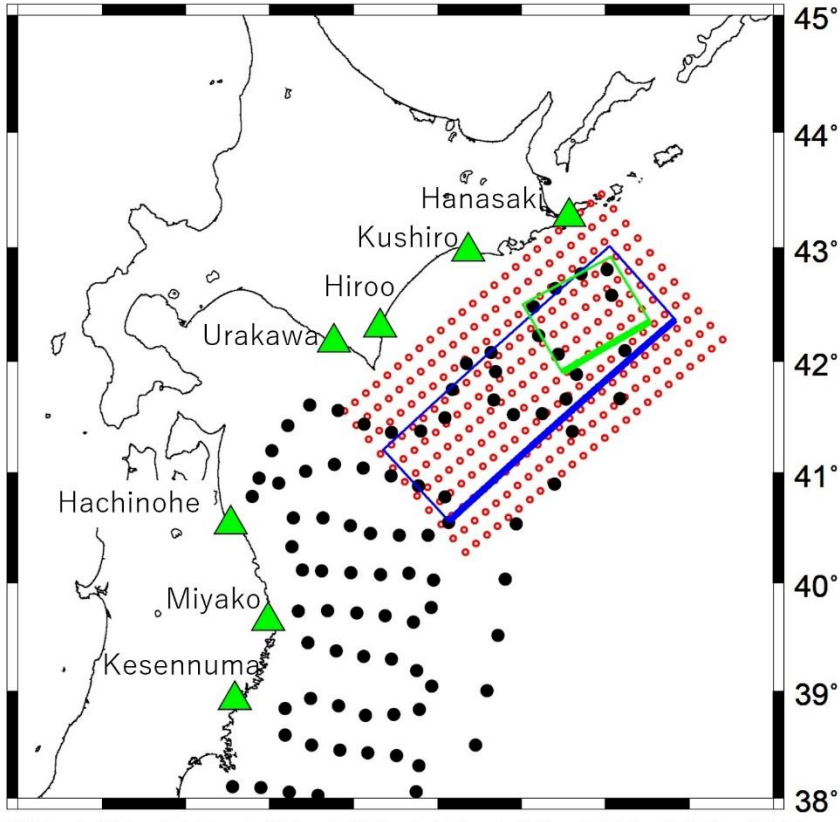
374

375



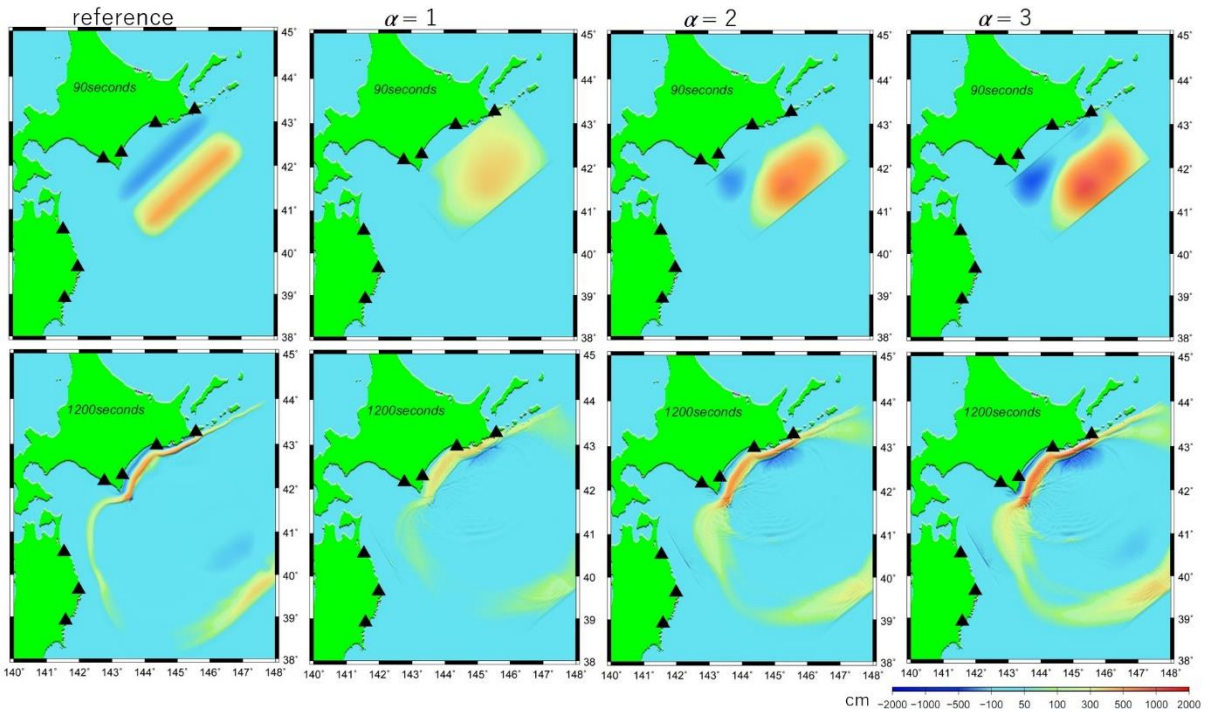
376

377 Figure 1.



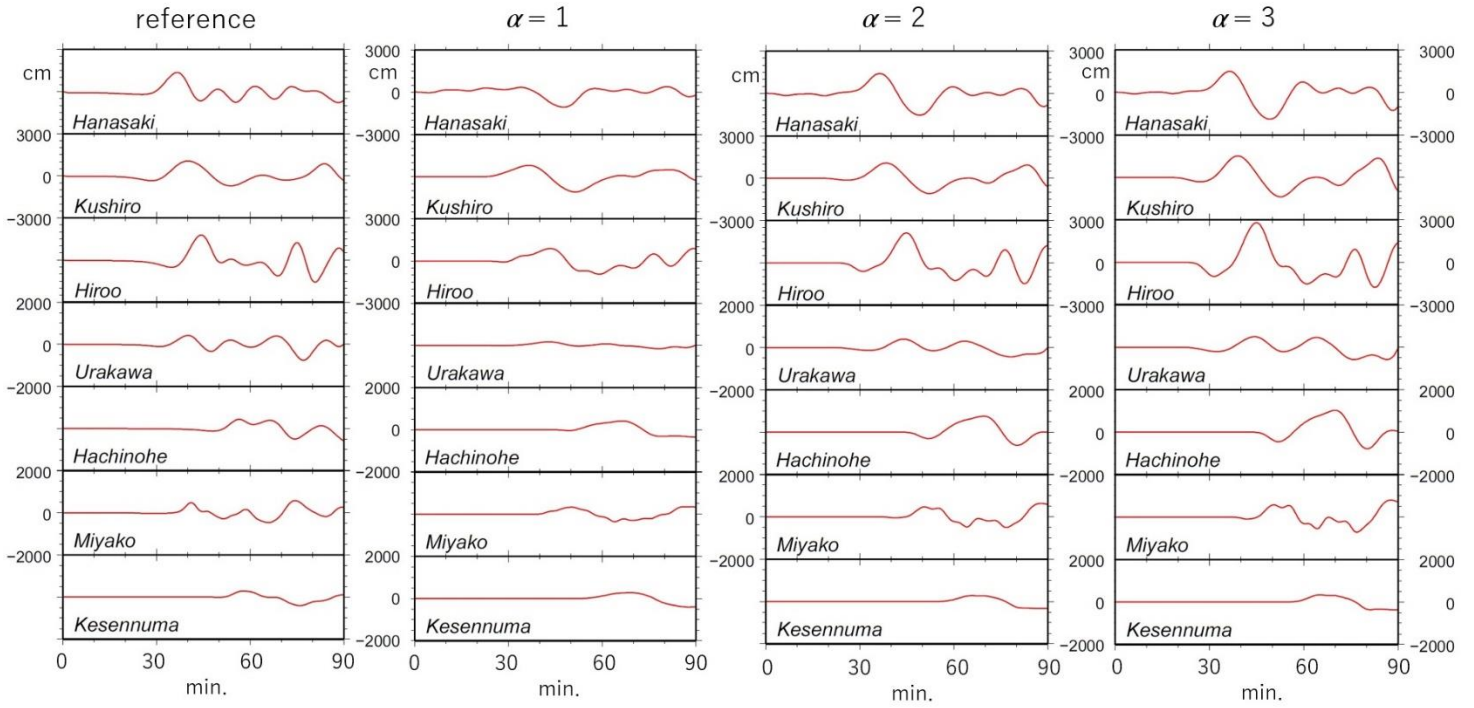
378 139° 140° 141° 142° 143° 144° 145° 146° 147° 148°

379 Figure 2.

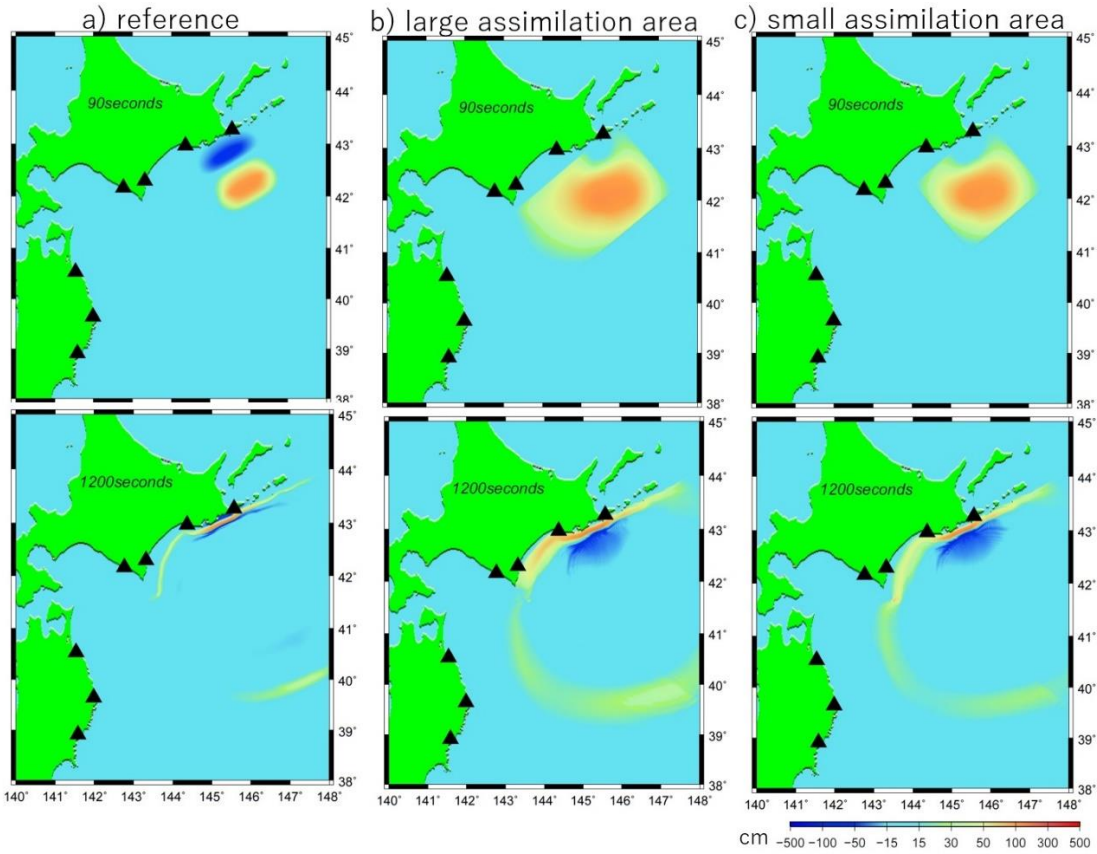


380

381 Figure 3.

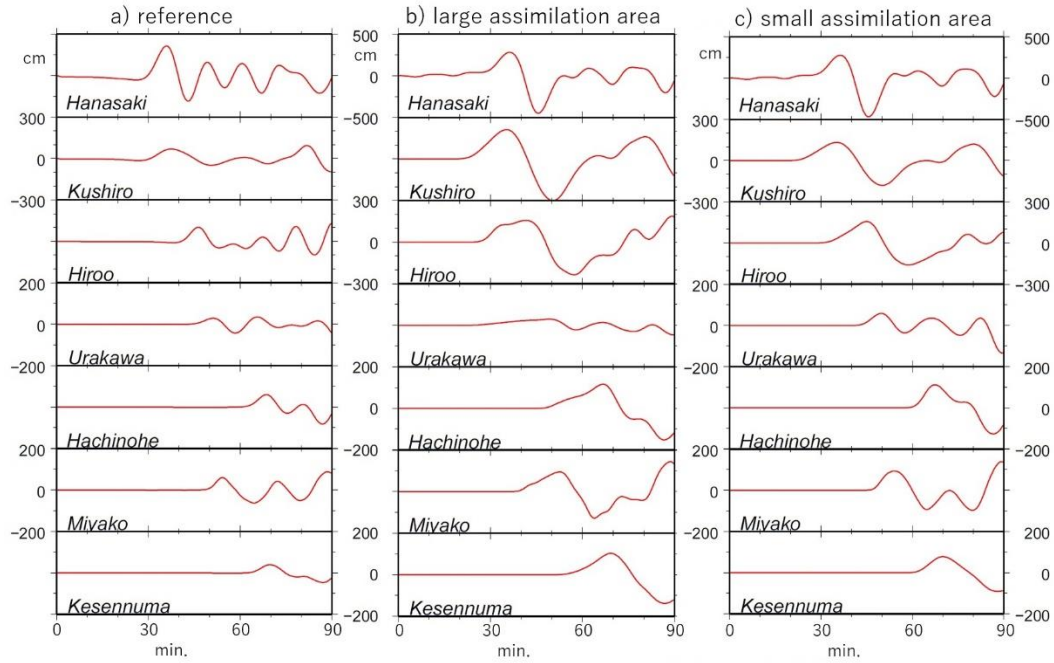


382 Figure 4.



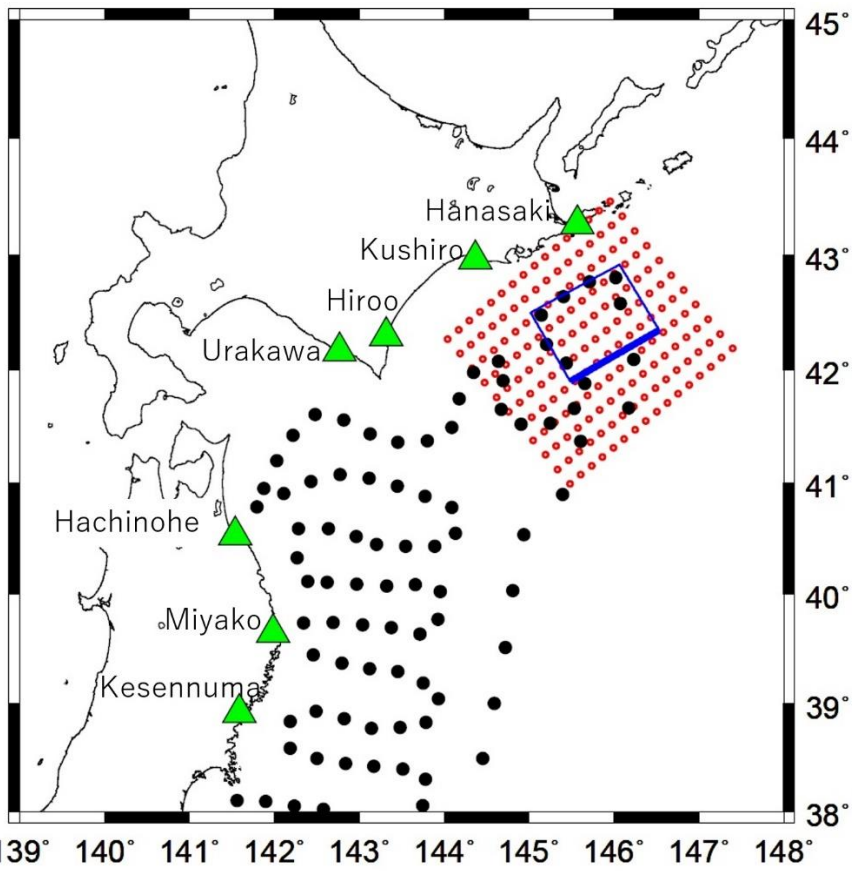
383

384 Figure 5.



385

386 Figure 6.



387

388 Figure 7.

# Figures

$$z_{i,j}^k = \frac{\sum_{p=1}^n w_{p,i,j} z_p^k}{\sum_{p=1}^n w_{p,i,j}}$$

Figure 1

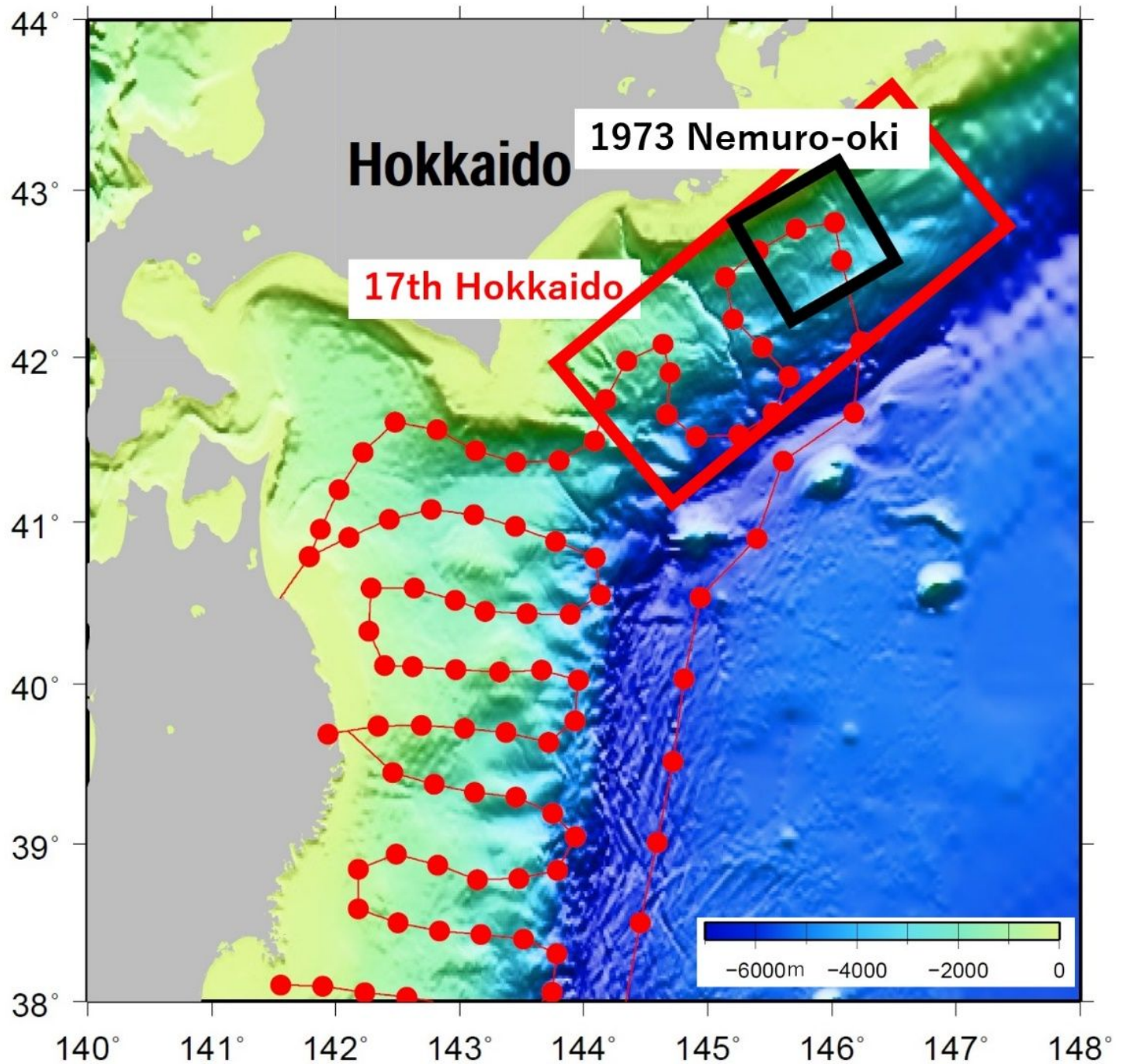


Figure 2

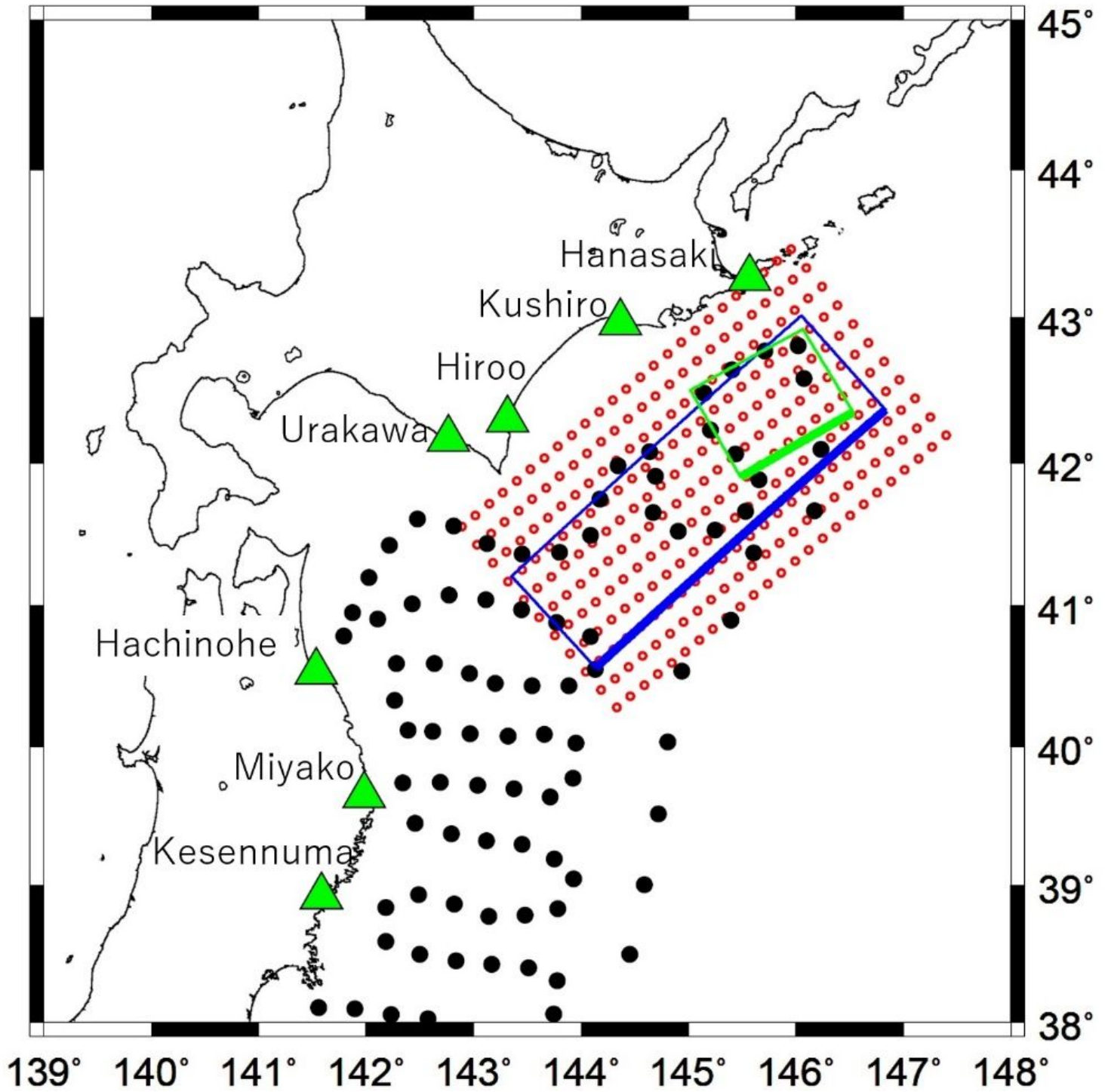


Figure 3

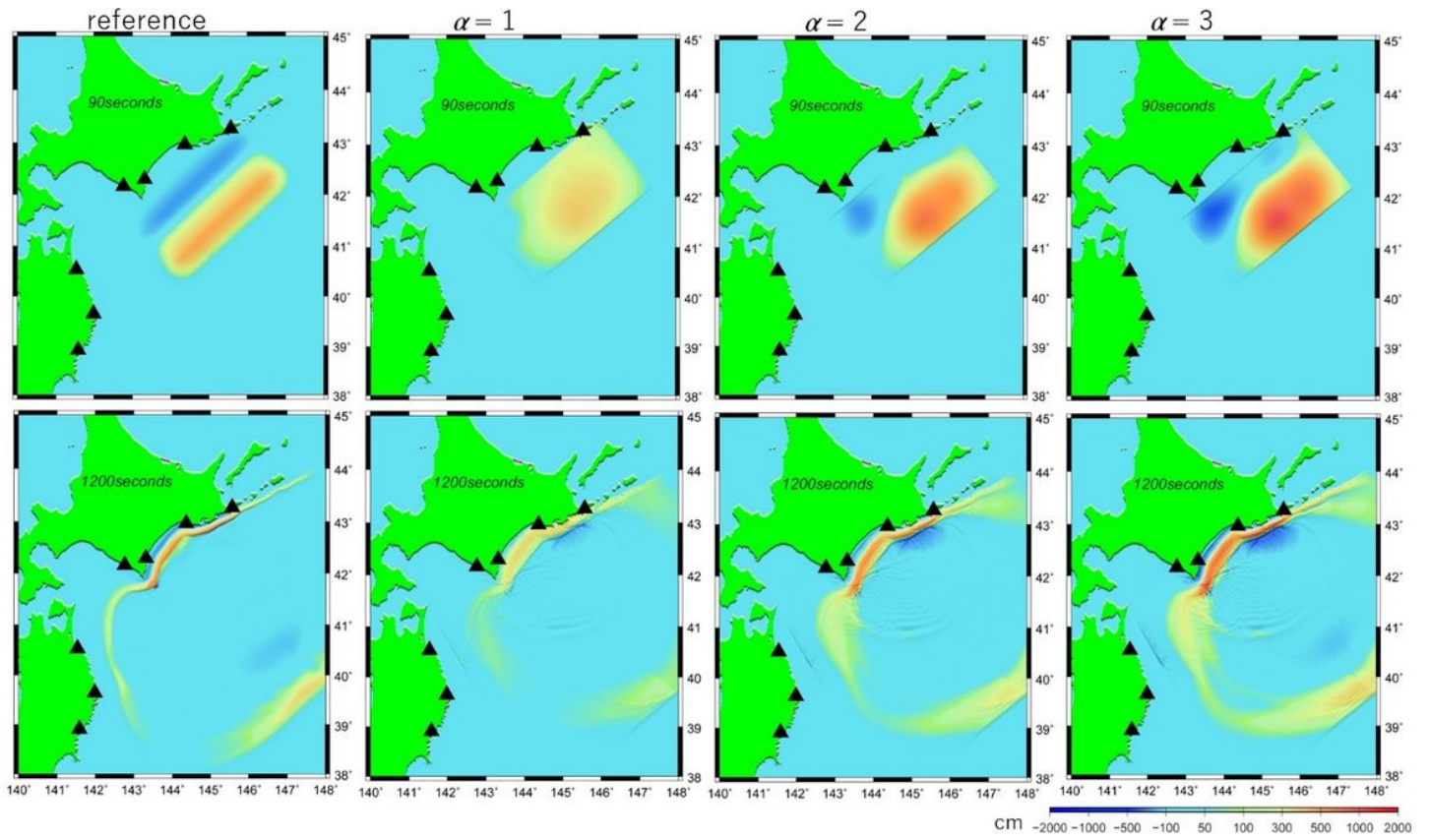


Figure 4

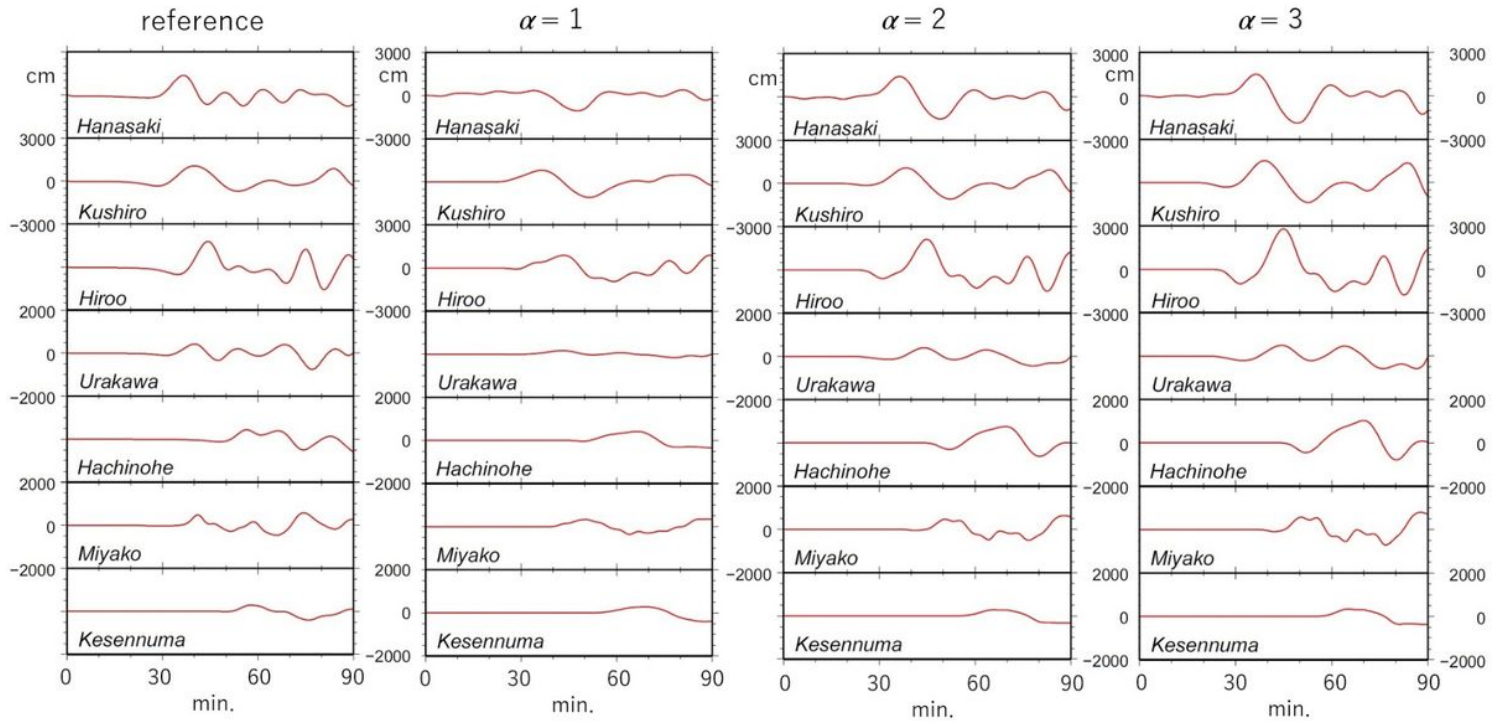


Figure 5

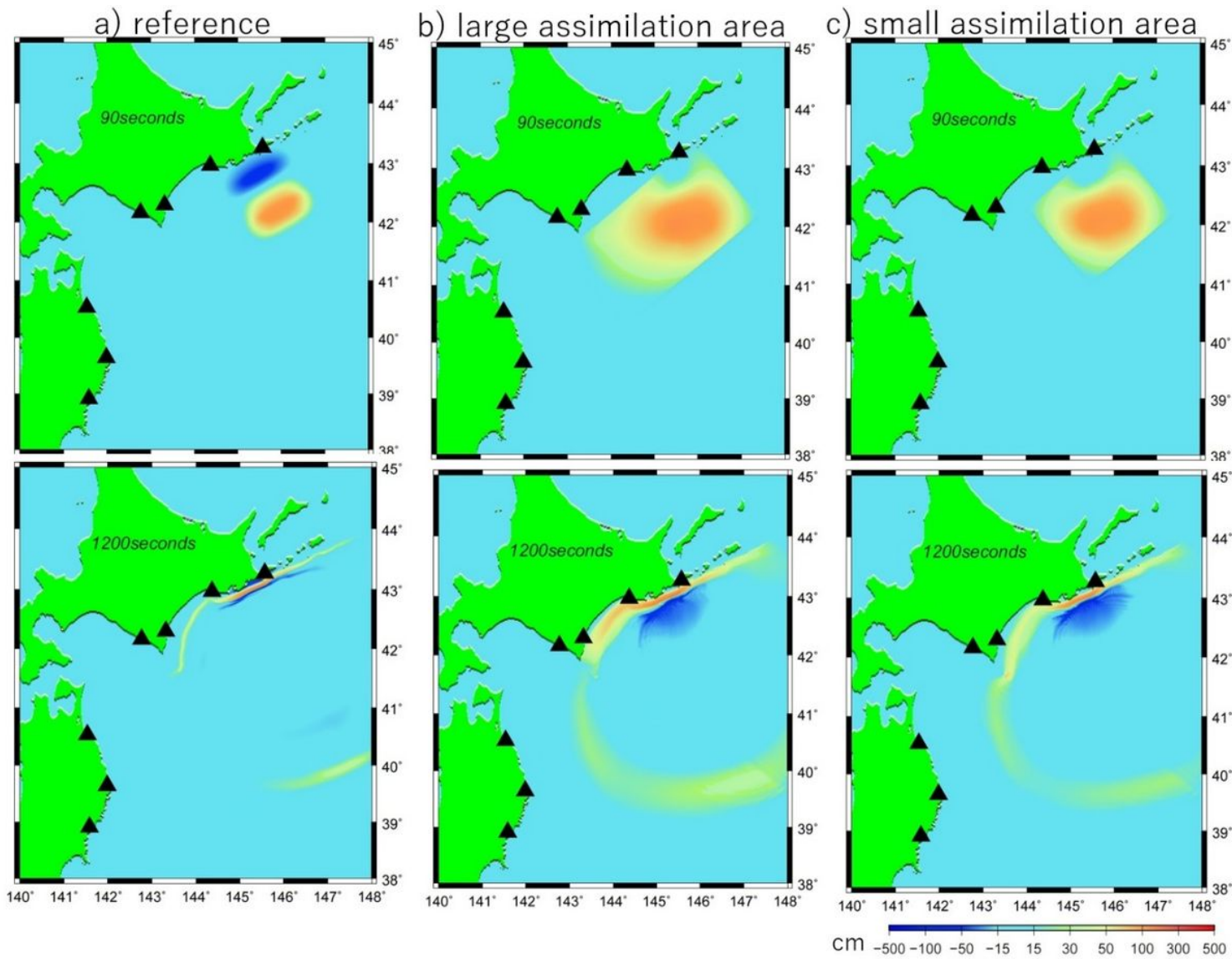


Figure 6

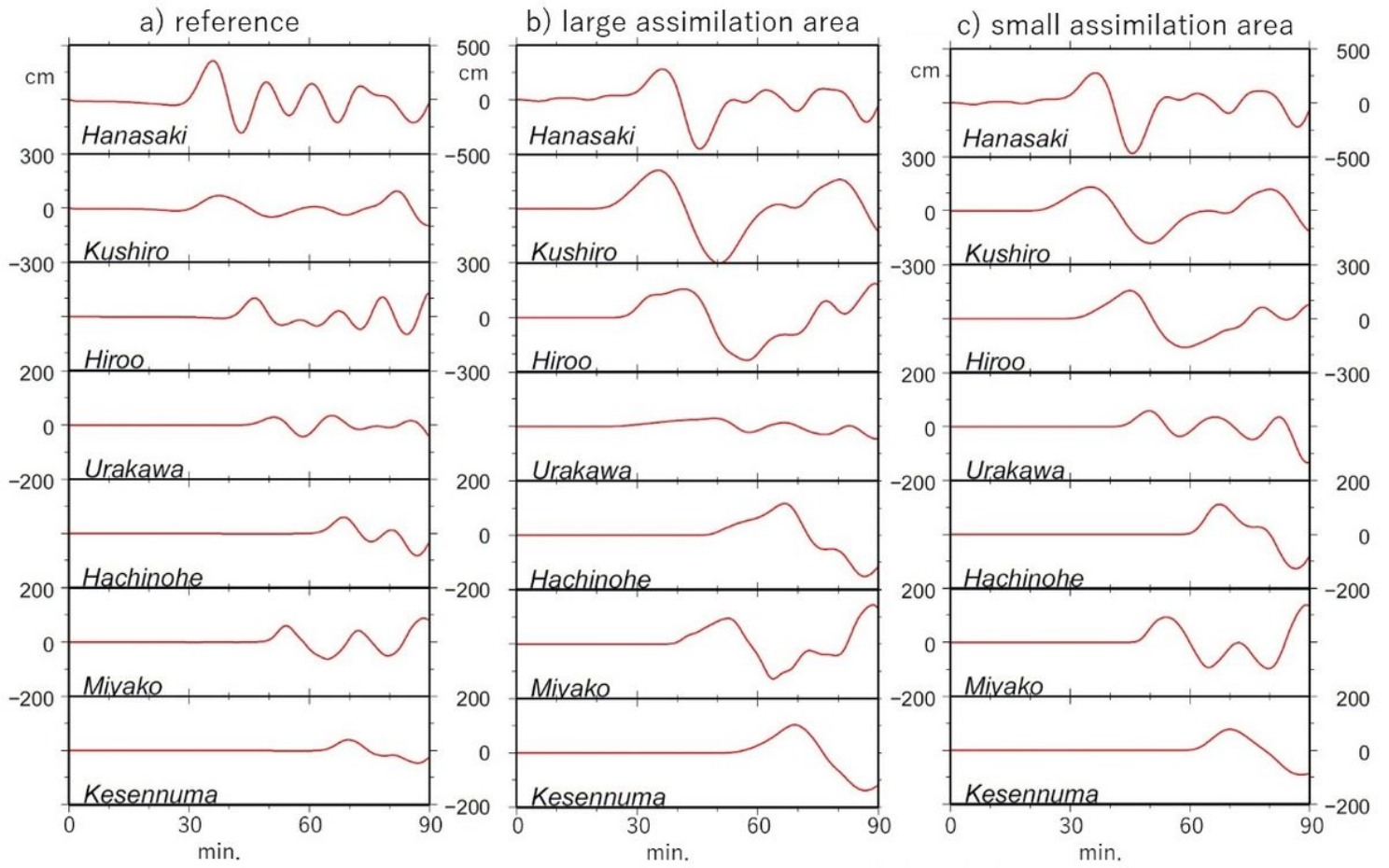


Figure 7

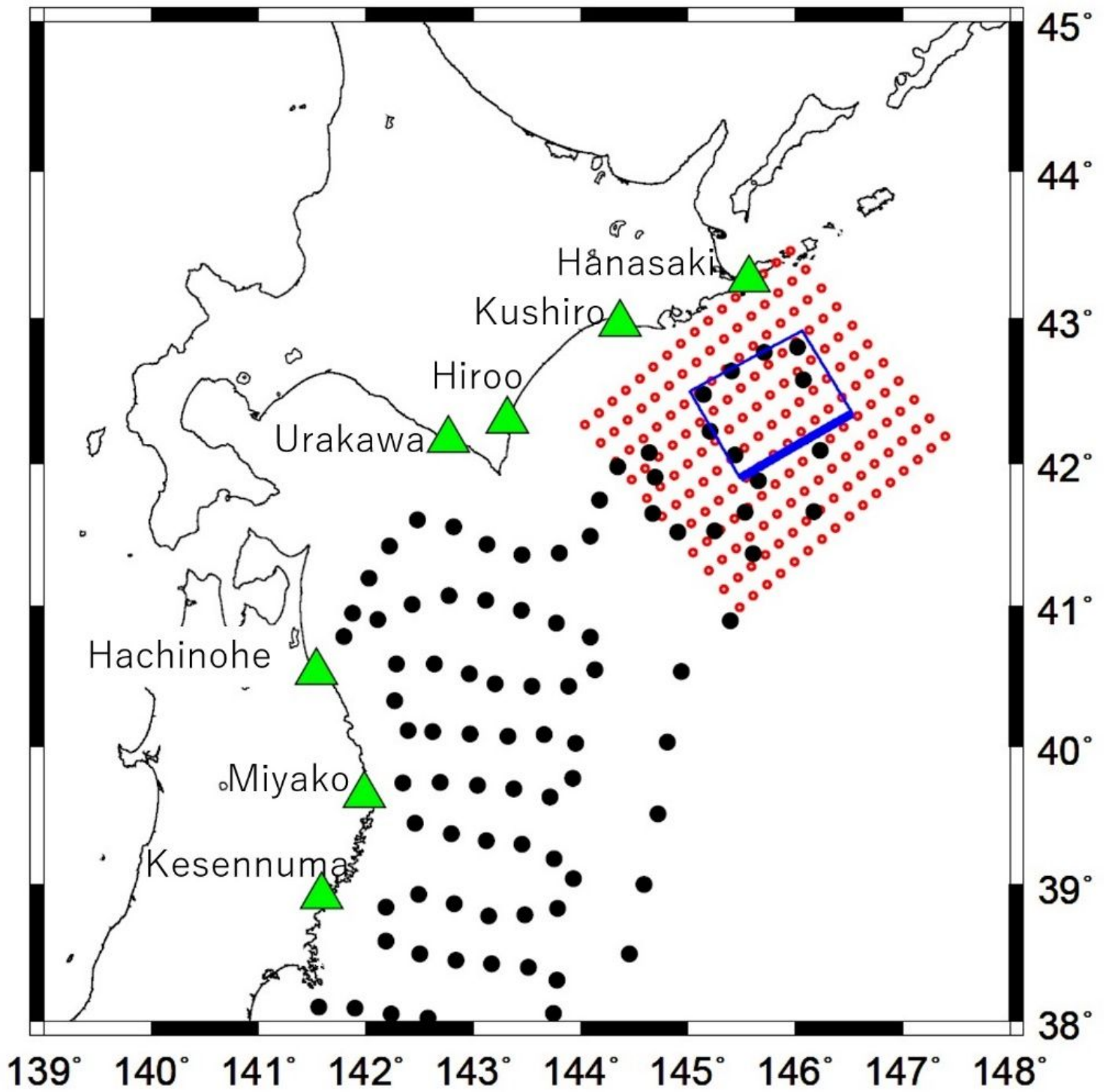


Figure 8

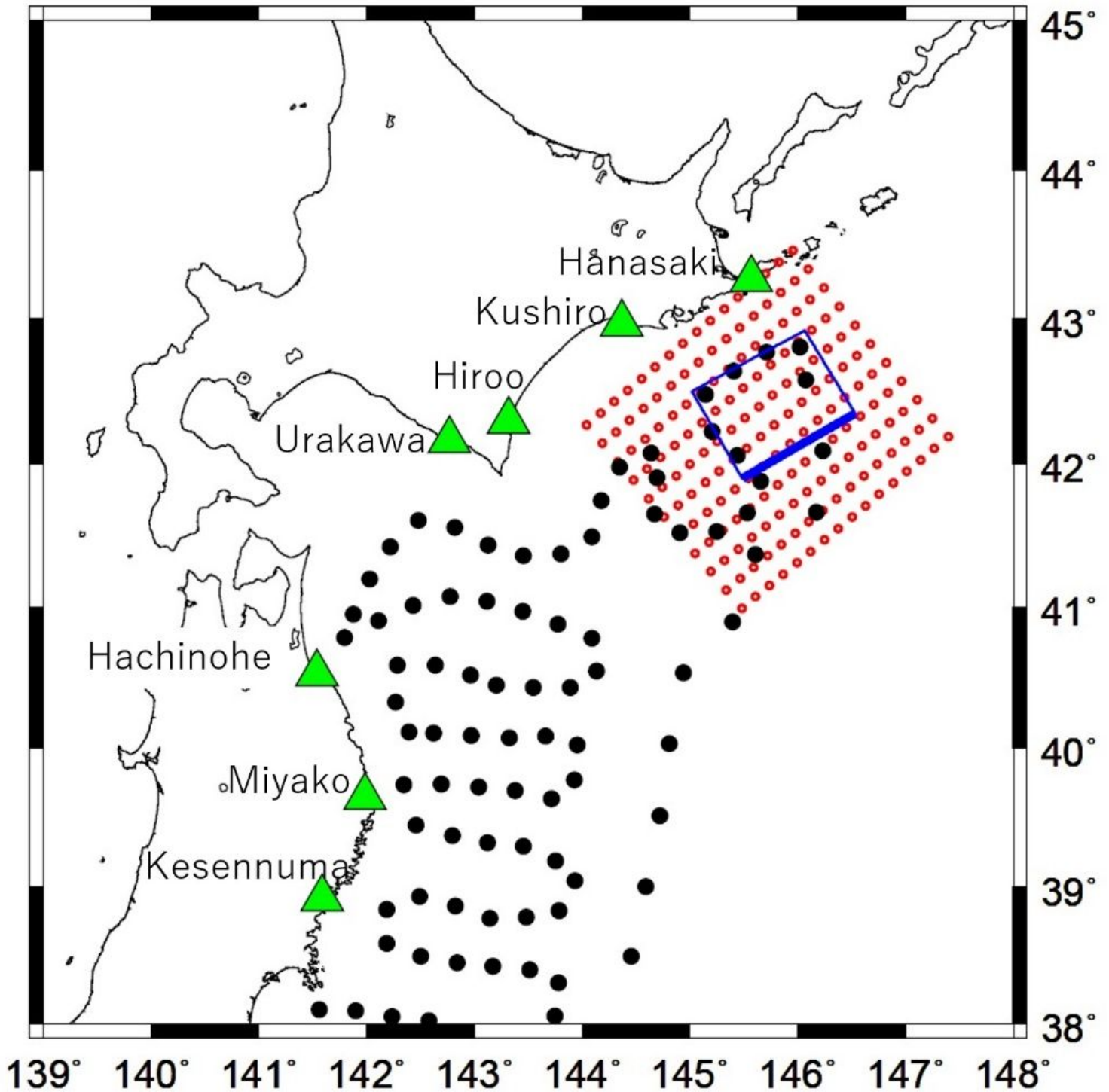
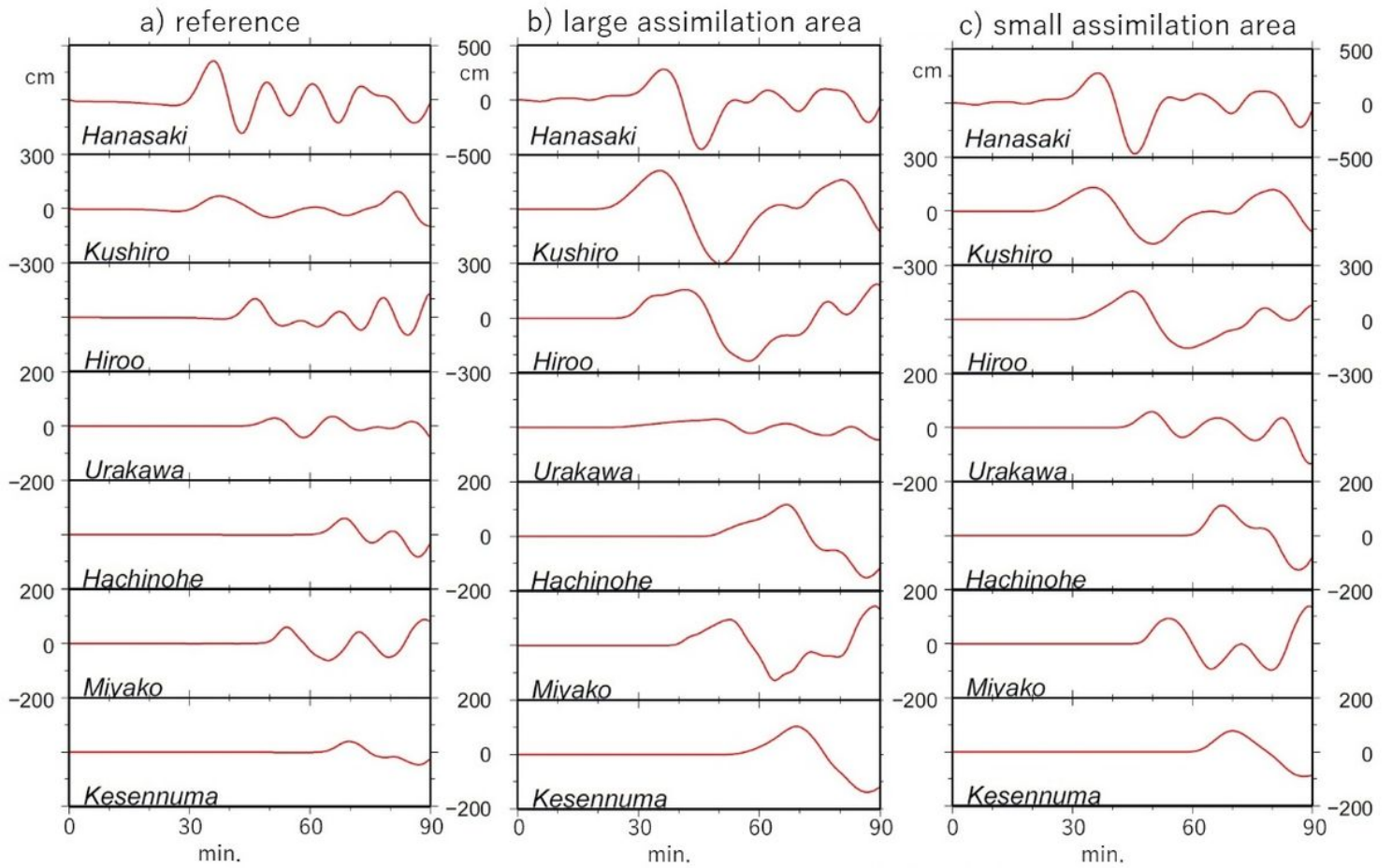


Figure 9

Locations of the assimilation data in a small assimilation area (marked by red dots) calculated by the interpolation of the observed data at the S-net sensors (black dots). The blue rectangle shows the test fault model of the Nemuro-oki earthquake (Mw8.0). Triangles demarcate the locations of the tsunami waveforms from Figure 6.



**Figure 10**

Comparisons of tsunami waveforms at seven locations (refer to Figure 2 for exact locations) for the reference tsunami (a) of the Nemuro-oki earthquake case and two assimilation tsunamis using a large assimilation area (b) (for exact locations refer to Figure 2) and a the small assimilation area (c) (for exact locations refer to Figure 7).

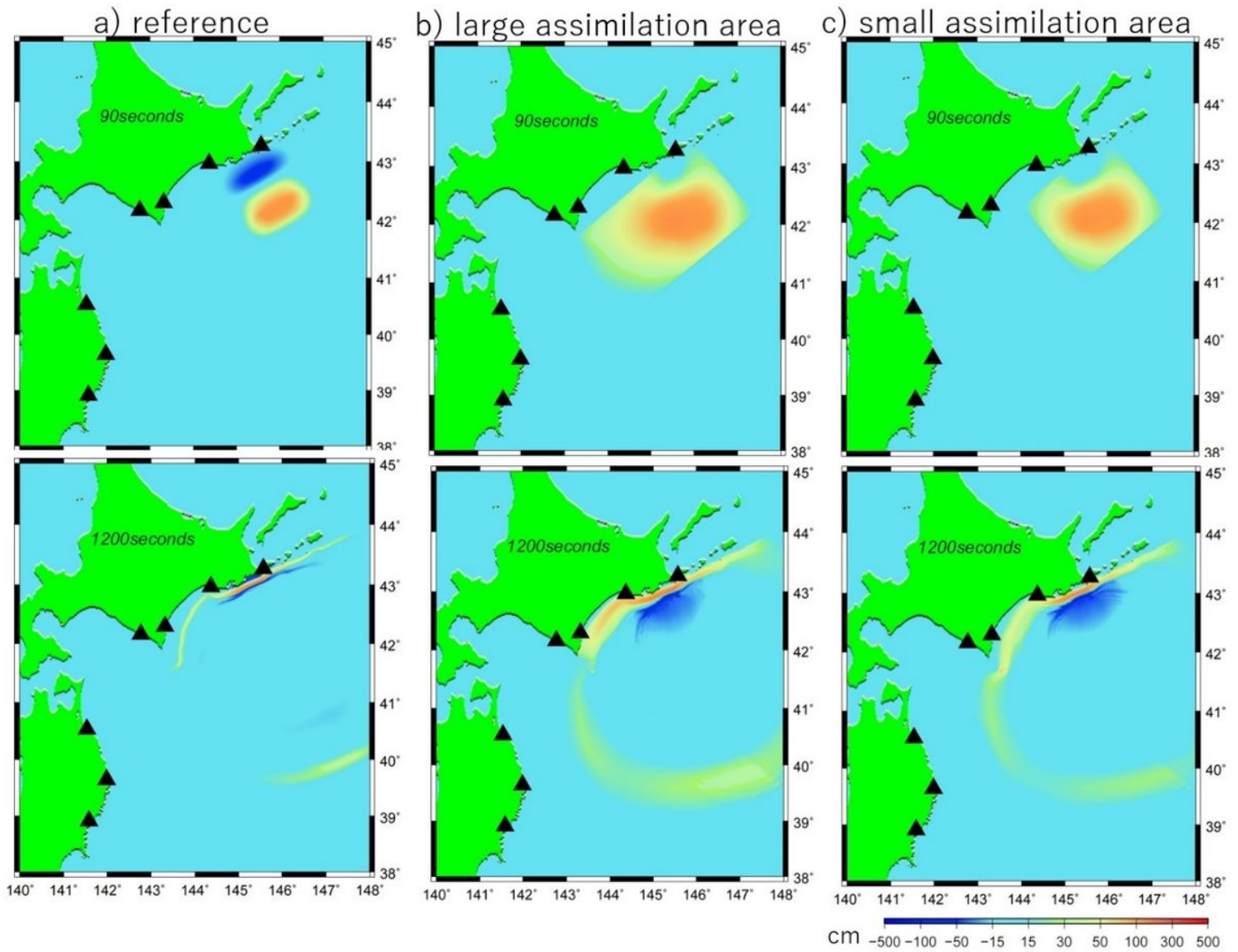


**Figure 11**

Comparisons of tsunami height fields 90 and 1200 s after the initiation of the earthquake for the reference tsunami (a) of the Nemuro-oki earthquake and two assimilation tsunamis computed using the interpolation of the simulated observation data at the S-net sensors for a large assimilation area (b) (for exact locations refer to Figure 2) and a the small assimilation area (c) (for exact locations refer to Figure 7).

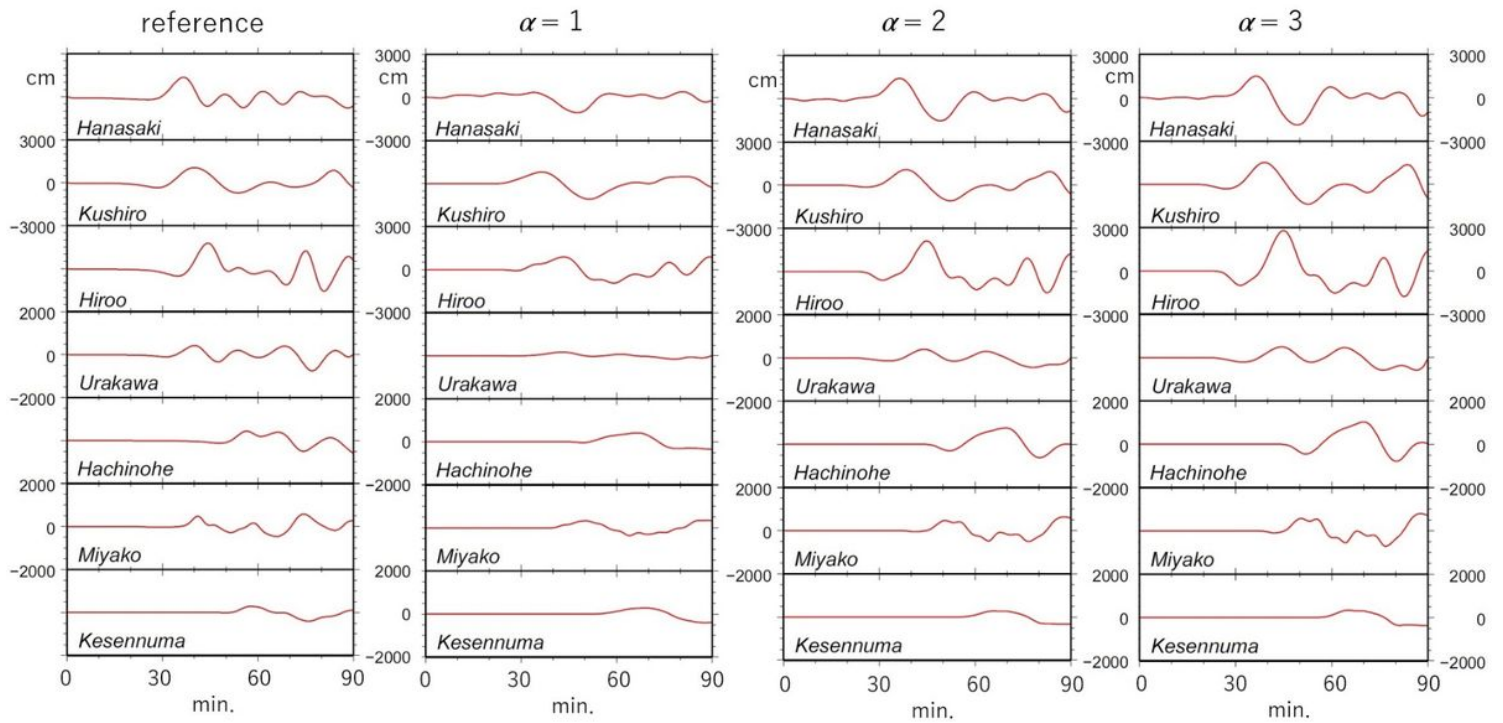


Figure 12

Comparisons of tsunami waveforms at seven locations (refer to Figure 2 for exact locations) for the reference tsunami of the giant earthquake and three assimilation tsunamis, where control factors  $\alpha$  from Eq. (4) ranges from 1 to 3.

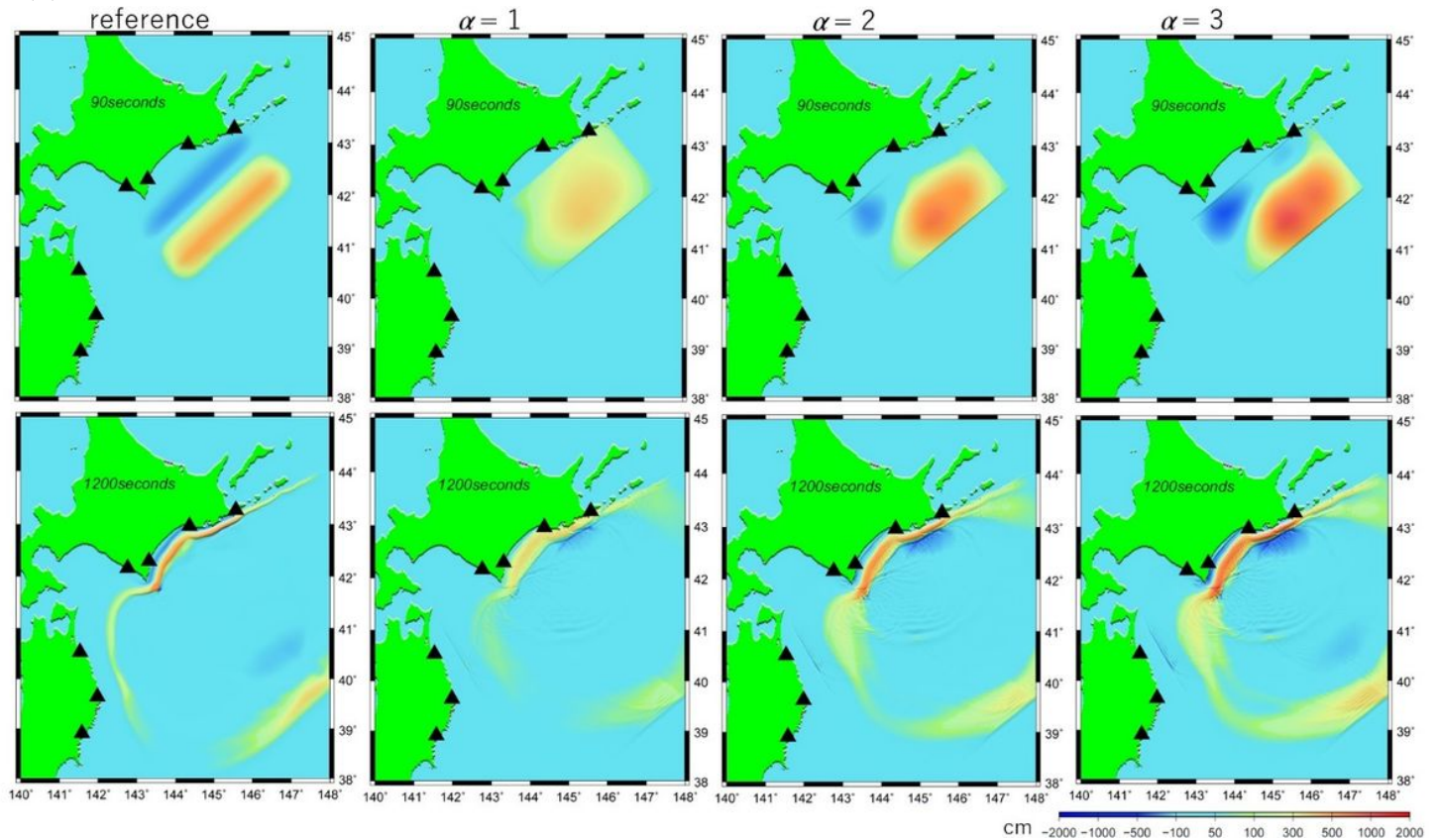


Figure 13

Comparisons of the tsunami height fields 90 and 1200 s after the initiation of the earthquake for the reference tsunami of the giant earthquake and three assimilation tsunamis as computed by the interpolation of the simulated observation data at the S-net sensors using Eq. (3), where control factors  $\alpha$  from Eq. (4) ranges from 1 to 3.

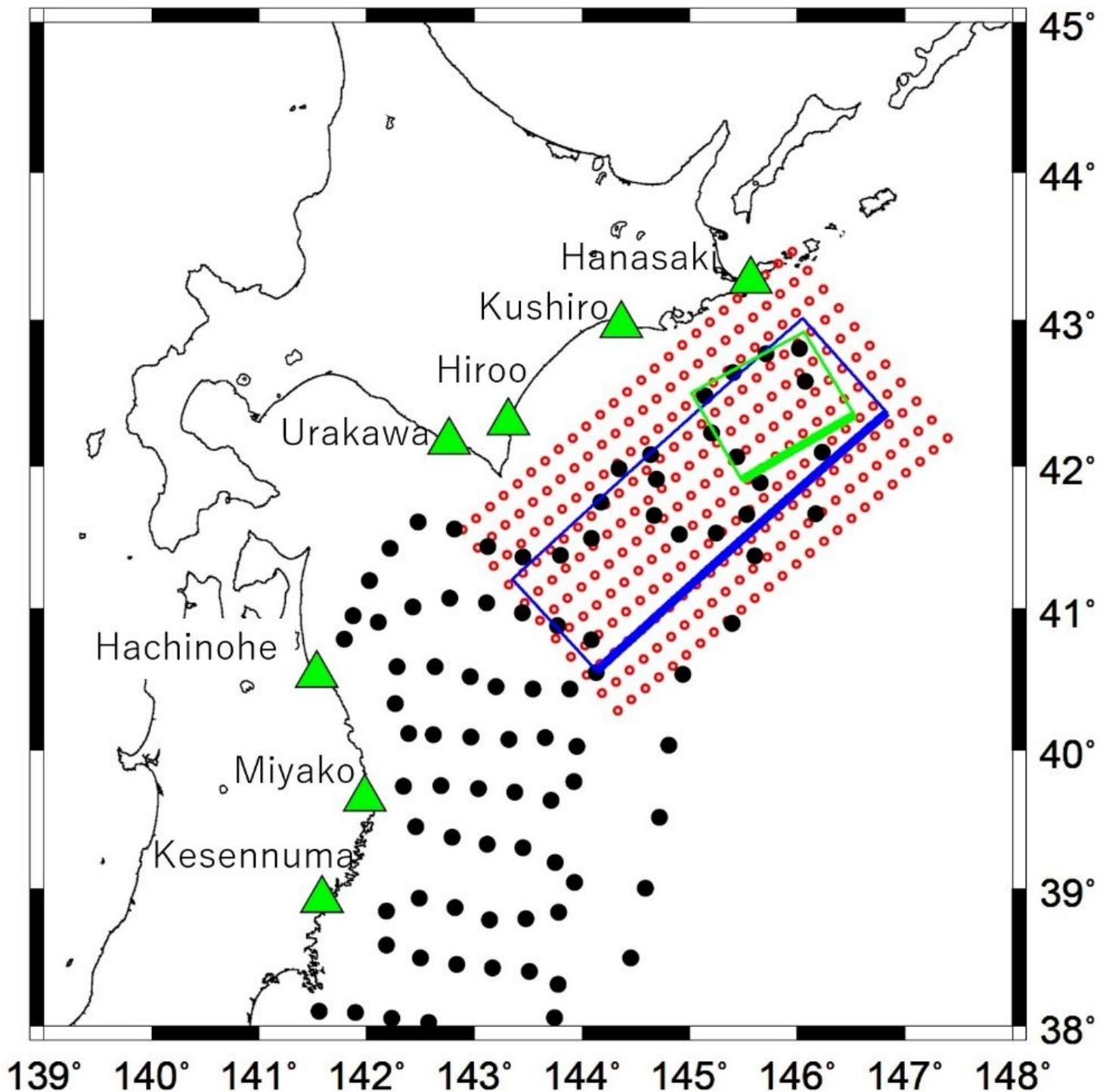
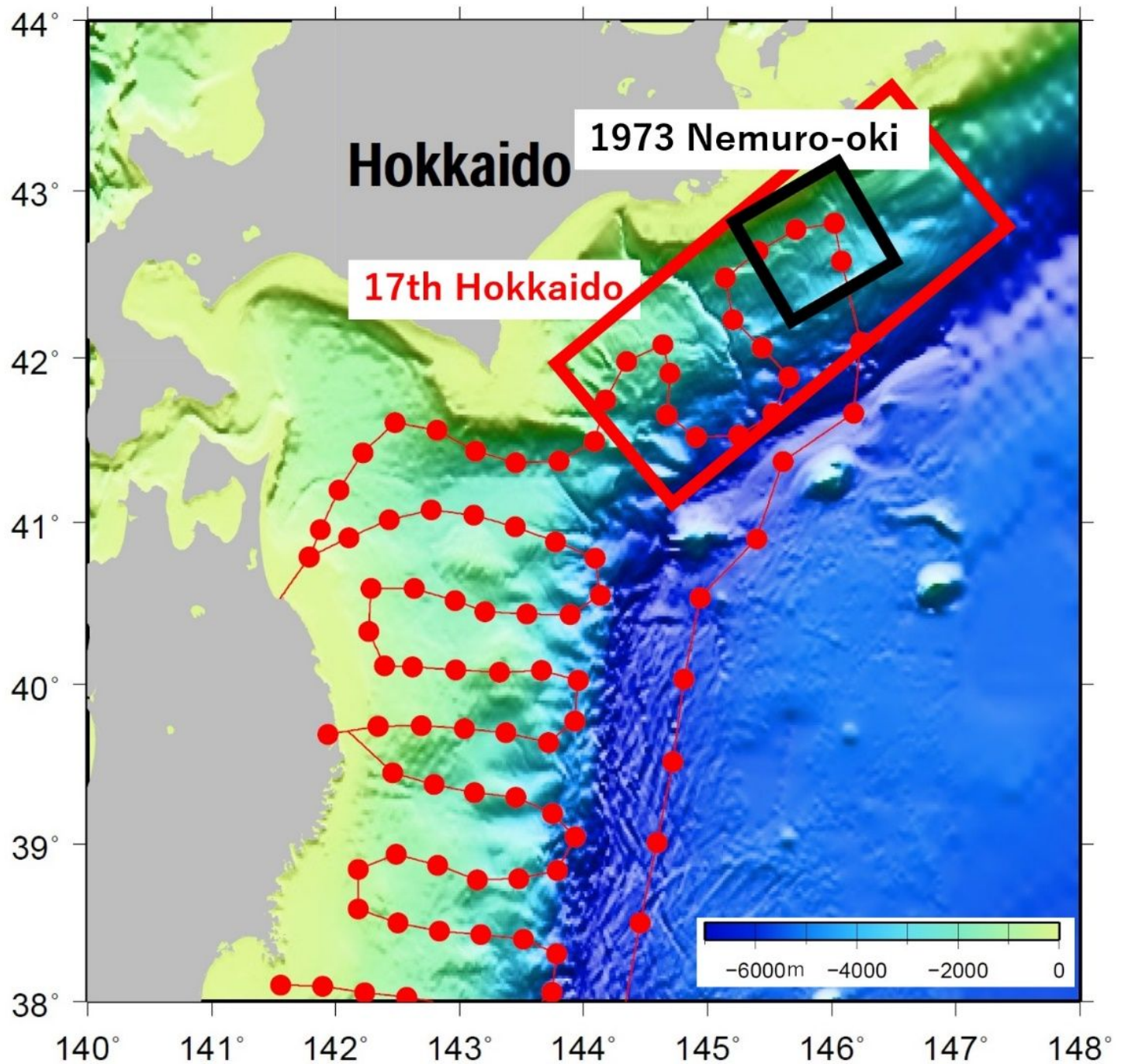


Figure 14

Tsunami simulation area and locations of the calculated assimilation data (red dots) using interpolation of the observed data at the S-net sensors (black dots). The blue and green rectangles show the locations of the two test fault models of the hypothetical giant earthquake (Mw8.8) and the Nemuro-oki earthquake

(Mw8.0), respectively. Triangles demarcate the locations where the tsunami waveforms are compared in Figures 4 and 6.



**Figure 15**

Bathymetry of the study area and locations of the S-net sensors (red dots). The red rectangle shows the source area of the 17th century giant earthquake (Mw 8.8), according to Ioki and Tanioka (2016). The black rectangle shows the source area of the 1973 Nemuro-oki earthquake (Mw 7.8), as per Tanioka et al. (2007).

## Supplementary Files

This is a list of supplementary files associated with this preprint. Click to download.

- [Graphic.jpg](#)